MATHEMATICAL BIOSCIENCES
AND ENGINEERING
Volume **3**, Number **4**, October **2006**

http://www.mbejournal.org/

pp. **697–716**

COMPLEX SPATIO-TEMPORAL FEATURES IN MEG DATA

Francesca Sapuppo [1], Elena Umana [1], Mattia Frasca [1]
Manuela La Rosa [2], David Shannahoff-Khalsa [3], Luigi Fortuna [1]
Maide Bucolo [1]

[1] Dipartimento di Ingegneria Elettrica, Elettronica e dei Sistemi
Universitá degli Studi di Catania, V.le A, Doria 6, 95125 Catania, Italy
[2] PST Group, Corporate R&D, STMicroelectronics, Catania site
Stradale Primosole 50, 95121 Catania,Italy
[3] Institute for Nonlinear Science, University of California, San Diego
9500 Gilman Dr., La Jolla, 92093-0402 CA

(Communicated by Stefano Bocaletti)

Abstract. Magnetoencephalography (MEG) brain signals are studied using a method for characterizing complex nonlinear dynamics. This approach uses the value of d_∞ (d-infinite) to characterize the system's asymptotic chaotic behavior. A novel procedure has been developed to extract this parameter from time series when the system's structure and laws are unknown. The implementation of the algorithm was proven to be general and computationally efficient. The information characterized by this parameter is furthermore independent and complementary to the signal power since it considers signals normalized with respect to their amplitude. The algorithm implemented here is applied to whole-head 148 channel MEG data during two highly structured yogic breathing meditation techniques. Results are presented for the spatio-temporal distributions of the calculated d_∞ on the MEG channels, and they are compared for the different phases of the yogic protocol. The algorithm was applied to six MEG data sets recorded over a three-month period. This provides the opportunity of verifying the consistency of unique spatio-temporal features found in specific protocol phases and the chance to investigate the potential long term effects of these yogic techniques. Differences among the spatio-temporal patterns related to each phase were found, and they were independent of the power spatio-temporal distributions that are based on conventional analysis. This approach also provides an opportunity to compare both methods and possibly gain complementary information.

1. **Introduction.** Brain activity is the expression of macroscopic patterns resulting from microscopic interactions of neuronal assemblies. While the activity of single neurons has been characterized through physiological studies and modeling [1][2], the macro-dynamics of whole brain neural activity are best studied using electroencephalographic (EEG) and magnetoencephalographic (MEG) signals. EEG and MEG measure macroscopic physical properties deriving from the cooperation of many neurons, and thus present an opportunity to study the relationship between the micro- and macro-levels of the brain. Studies in the literature deal mainly with the temporal aspects and the evolution of synchronization using mostly coherence and phase locking [3]. Various linear and nonlinear analysis techniques are described

2000 *Mathematics Subject Classification.* 92D30.
Key words and phrases. complexity, Magnetoencephalography, d-infinite (d_∞).

in the literature for studying MEG and other brain signals in an attempt to characterize normal resting activity, effects of sensory stimulation, and pathological states [4][5][6][7]. Nonlinear multivariate time series analysis is also used in neurophysiology with the aim of studying the relationship between simultaneously recorded signals [8]. These signals are frequently characterized using the standard nonlinear measures of the Lyapunov exponents and the correlation dimension [9][10]. The computation of these parameters on time series involves the concepts of time-delay embedding. The reconstruction of the state space, thus requires using a time lag and embedding dimension [11].

In the work presented here, the technique is based on the evaluation of the asymptotic distance d_∞ (d-infinite)[12][13], and this measure has been studied for characterizing nonlinear dynamics in experimental data. A novel implementation to evaluate d_∞ is introduced and this method is computationally less onerous then the conventional methods, since it is not based on the time-delay embedding concept and no intermediate computational steps are needed to obtain the final result. This method may also fulfill the requirement of being general and applicable for experimental data derived from other instruments used in experimental diagnostics, including EEG, ECG, etc. This approach may also prove to be computationally efficient so that it can also be used by both clinicians and researchers.

In general, in the theoretical determination of the λ and d_∞, knowledge of the finite difference equations in the discrete domain as well as the differential equations in the continuous domain is fundamental. An example of evaluation of d_∞ for known nonlinear systems has been reported in the literature, particularly, in relation to the Chua circuit [12][13].

When the laws of the systems under study are unknown and we are provided only with experimental data, the need arises for a calculation of the asymptotic distance d_∞ for generic time series. Therefore, the novel procedure developed here evaluates the d_∞ as the asymptotic value of the average distance between trajectories that are extracted directly from the time series.

As a preliminary study, the theoretical and methodological framework has been tested and verified. The extraction of the d_∞ parameter has been performed on numeric series coming from well-known nonlinear systems showing chaotic behavior. It was also tested on periodic time series and on random white noise as a baseline. It was the first step for a study focused on characterization of the robustness of the d_∞ parameter to the addition of Gaussian noise to the signal.

Furthermore, to verify the consistency of the methodology, a comparison was performed between the computation of the d_∞ on trajectories of a discrete map, starting from nearby points, and the computation of it on short sequences, starting from nearby values in a long-run numeric series generated by the same discrete map.

The approach for the d_∞ extraction from time series has been used here with MEG signals to help characterize the occurrence of spatio-temporal patterns in the brain. Specifically, we exploit the potential of the d_∞ parameter for data analysis, comparing these results to the power distribution analysis. Low-power activities are also vital for decoding brain activity. Therefore, there is a need for studying new parameters to emphasize spatially distributed dynamics that are not necessarily related to high power neuronal activity.

This method has been applied here with a subject performing a highly structured yogic breathing technique that previously showed efficacy for the treatment

of patients with obsessive compulsive disorder (OCD) [16]. This analysis compares brain activity in the different phases of the protocol and correlates it with the potential effects of the breathing exercise. Multiple data sets are analyzed to help detect any potential long term brain effects using these yogic techniques.

2. **Case study.** Recordings were made using a whole-head 148-channel MEG instrument (4-D Neuroimaging, San Diego, California) located at The Scripps Research Institute (La Jolla, CA). Each of the 148 pick-up coils in this instrument is a 2-cm diameter magnetometer, with a distance of 2.2 cm between coils, center to center. Each coil is connected to a SQUID that produces a voltage proportional to the magnetic field radial to the head, resulting in preferential sensitivity to neural electrical sources tangential to the surface of the scalp emanating from cortical sulci. This MEG system is contained in a magnetically shielded room that helps reduce the contribution of magnetic fields from more distant sources, and this significantly increases the signal-to-noise ratio and improves the ability to detect deeper signal sources in the brain. Trained MEG technicians positioned the subject, applied electro-oculogram leads, and performed head shape digitization. An individual was employed who is highly trained with yogic breathing techniques and used to MEG recordings protocols. Head-shape was digitized, based on known locations on the subject's head (tragus of left and right ears and nasion). Head shape data is for later co-registration between measurement coil locations, electrode locations, and scalp landmarks (Figure 1 (a),(b)). Eye movements were recorded with electrodes placed above and below the right eye. Electrode impedances were set below 5 kohms. MEG data was recorded with a sampling rate of 251 Hz, with an analog filter band pass of 1 to 100 Hz.

2.1. **Yogic protocol.** The subject was recorded while reclining and supported at 45 degrees. The subject followed a well-practiced protocol (see Figure 2) that involves 10 minutes of resting baseline recording (rest phase I), followed by a 31-minute exercise recording phase, and then followed by 10 minutes of resting recording (rest phase II). The three phases are separated by a one-minute recording pause.

The exercise phase consists of selectively breathing through only one nostril (using a plug for the other side, with both arms resting in the lap) at a respiratory rate of one breath per minute (15 s slow inspiration, 15 s breath retention, 15 s slow expiration, and 15 s breath hold out) [15]. On day one the technique employing the left nostril is used (the pattern that has shown efficacy in treating OCD [16]), and on the following day, the same pattern was employed using the right nostril. This approach is used to study the potential differential brain effects that may result from these two unique meditation techniques, and to help insure that the effects of one technique do not carry over into the effects of the other that may occur if both techniques were practiced on the same day. Three two-day experiments are repeated with a time lag of approximately one month. The date and left or right nostril recordings are presented in Table 1.

2.2. **Power study on MEG signals.** A study of the spatio-temporal power distribution was performed on the MEG data collected in this subject while performing the two different yogic breathing exercises [17]. Power analysis is performed to characterize the distribution on the scalp using the maximum of the autocorrelation functions for all channels. The autocorrelation function, represented in equation

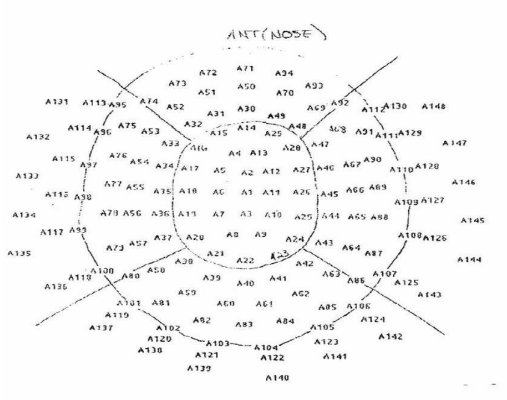

(a)

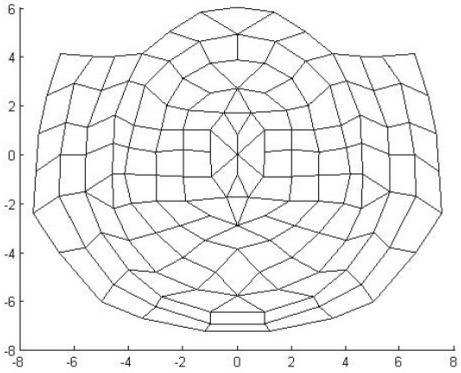

(b)

FIGURE 1. Spatial distribution whole head MEG channels on the scalp. (a) Numeric code and position of the channels. (b) Digital head reconstruction via software (Matlab).

TABLE 1. Experimental data sets over a three-month time period

Left nostril	**Right nostril**
June 13, 2000 - 5	June 14, 2000 - 6
July 18, 2000 - 7	July 19, 2000 - 8
August 8, 2000 - 9	August 9, 2000 - 10

(1) as $C_i(k)$, is calculated on one-minute time series (N samples) for each channel ch_i, and the value in zero $C_i(0)$ represents the power of the signal in that minute.

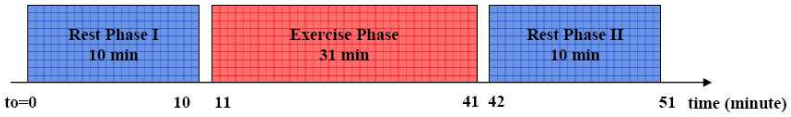

FIGURE 2. Yogic Protocol Timeline.

$$C_i(h) = \frac{1}{N} \sum_{k=1}^{N-1} ch_i(k) ch_i(k+h). \tag{1}$$

The two spatio-temporal maps in Figure 3 are for the left (a) and the right nostril (b) breathing protocols respectively (data sets 5 and 6 in Table 1), and they illustrate the entire whole-head MEG power as it evolves over one minute intervals. The color of the pixel (j^{th},i^{th}) represents the value of the power intensity related to the j^{th} minute for the i^{th} channel, using a conversion that is described by the color-bar on the right of the image. Thus, the image's i^{th} column represents the time evolution by one-minute time-windows of the MEG signals power at the i^{th} channel.

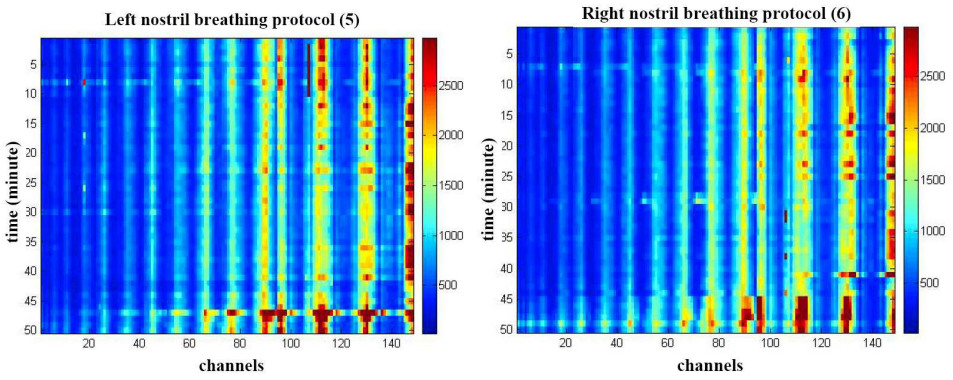

(a) (b)

FIGURE 3. Spatio-temporal power maps. (a) Left nostril breathing protocol(5). (b) Right nostril breathing protocol (6).

It is worth noting the emergence of patterns in the maps for the single-channel columns. Some differences can be observed in the three different phases of the yogic protocol and in the different channels during the different phases. To help illustrate these changes in the spatial patterns more clearly, head power maps are reconstructed for each phase of the data sets 5 and 6, as shown in Figure 4. In particular, the power spatial distribution of each phase is the result of an averaging process on the number of minutes belonging to the respective phase.

Defining as P_{ji} the power of the i^{th} channel signal relative to the j^{th} minute, which is represented by the j^{th}, i^{th} element of the maps in Figure 3, the spatial head maps relative to each phase were obtained by averaging the P_{ji} over each phase period, as follows:

$$P_i^{rpI} = \sum_{j=1}^{10} P_{ji} \tag{2}$$

$$P_i^{ep} = \sum_{j=11}^{41} P_{ji} \tag{3}$$

$$P_i^{rpII} = \sum_{j=42}^{51} P_{ji}, \tag{4}$$

where rpI stands for rest phase I, ep for exercise phase and rpII for rest phase II, and where $i = 1, 2, 3, .., 148$. To obtain the three head power maps in Figure 4 (a)-(c) for the left nostril protocol (data set 5) and in Figure 4 (d)-(f) for the right nostril protocol (data set 6), the P_i^{rpI}, P_i^{ep}, P_i^{rpII} are mapped using a color code for the power at the i^{th} intersection point of the mesh on the digital reconstruction of the coils positions (Figure 1(b)). The color values in the intermediate areas of the mesh are obtained through linear interpolation between neighboring points.

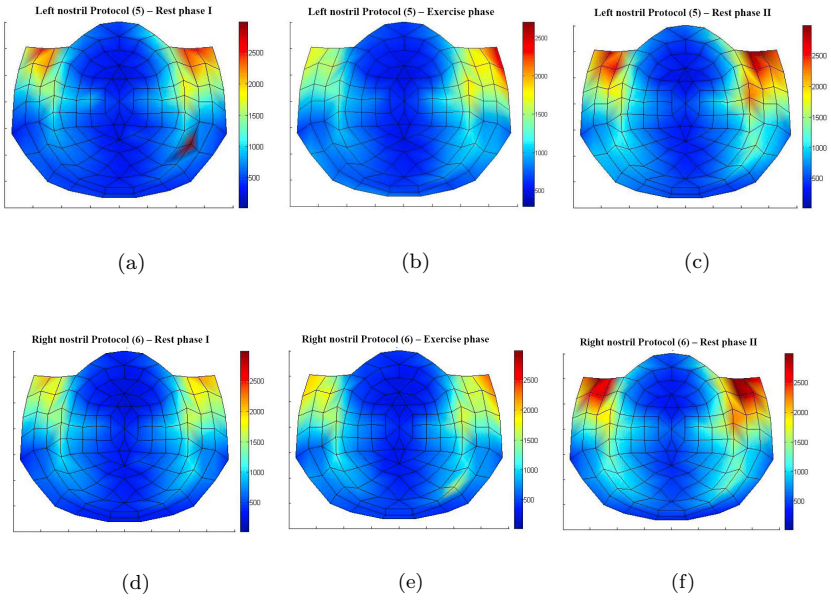

FIGURE 4. Power head map. Left nostril breathing protocol (5). (a) Rest phase I. (b) Exercise phase. (c) Rest phase II. Right nostril breathing protocol (6). (d) Rest phase I. (e) Exercise phase. (f) Rest phase II.

Some residual effects are visible in the rest phase II, which shows a more intense activity for both temporal lobes compared to the rest phase I in both experiments

regardless of the active nostril (Figure 4). The activity in the rest phase II is also spread more toward the temporal and occipital lobes.
It is possible to notice differences between the exercise phase and the two *rest phases*; Figure 5 shows the difference between the power distribution of the exercise phase and rest phase I for both protocols (left nostril (a), right nostril (c)) and the difference between the rest phase II and the exercise phase (Left nostril (b), right nostril (d)).

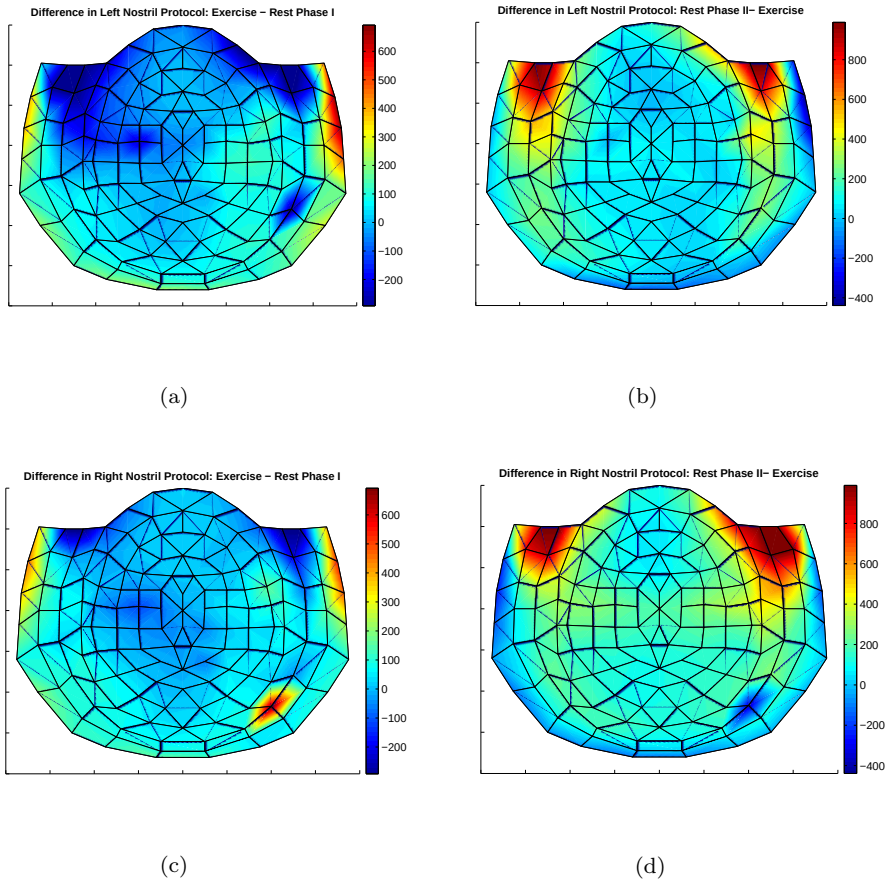

FIGURE 5. Difference between the power head maps between phases for the two different breathing protocols. Left nostril protocol: (a) Exercise phase minus rest phase I; (b) Rest phase II minus exercise phase. Right nostril protocol: (c)Exercise phase minus rest phase I; (d) Rest phase II minus exercise phase.

The residual effects of the rest phase II compared to the *exercise phases* mainly affects the frontal lobes where, as it is shown in Figure 5, a greater activity is present.
In particular, asymmetric activity occurs during the *exercise phases* when the right temporal lobe is more active than the left one, as shown in the two probability

distributions histograms of the power for the right and the left hemispheres in Figure 6 for the two different protocols.

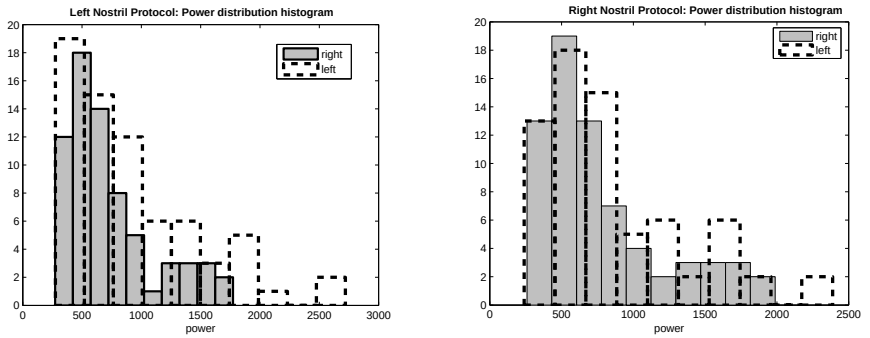

(a) (b)

FIGURE 6. Probability distribution histograms for the power during the exercise phase: right hemisphere (solid line-gray),left hemisphere (dashed line-white). (a) Left nostril protocol; (b) right nostril protocol

The averaging procedure on the phases' time window allows filtering random short-term noise, and, furthermore, both visualizations of the brain dynamics (spatio-temporal map and spatial head maps) allow a cross check in order to take into account possible measurement artifacts such as a temporary malfunction of specific channels. This is the case occurring in the first ten minutes of the left nostril breathing protocol (data set 5) shown in Figure 3 (a) represented by the dark red column in the upper part of the image, in correspondence of the channel A107 that is also visible as a dark red spot in the head map in Figure 4 (a).

3. Time series characterization through d_∞.

3.1. **Theoretical background.** Two key aspects of chaos are the stretching of infinitesimal displacements and the existence of complex orbit-like structures, in the form of a vast variety of possible unstable orbits, confined in a region of the phase space called the attractor. The stretching property is related to a sensitive dependence on initial conditions. The study on the system's trajectories and their time evolution according to their initial conditions represents a conventional methodology to characterize both continuous and discrete nonlinear systems and their dynamics [12][13][14].

Since the final objective of this paper is the characterization of discrete data, attention is focused on the mathematical formalization of the trajectory study in the discrete domain. Let us thus consider the map $x_{j+1} = G(x_j)$ with $x \in R$ and N pairs of trajectories at the j^{th} iteration ($x_j^{(i)} = G(\bar{x})$, $x_j^{\prime(i)} = G(\bar{x} + d_0)$) starting from two nearby points separated by a small distance d_0 in the boundary of the initial condition $\bar{x}$, and let us study how their distance evolves through the iterations.

The distance between the i^{th} pair at the j^{th} iteration ($d_j^{(i)} = |x_j^{(i)} - x_j'^{(i)}|$) is calculated for all the N pairs. Then the average value of d_j is calculated as follows in equation (5):

$$d_j = \frac{1}{N} \sum_{i=1}^{N} d_j^{(i)}. \tag{5}$$

The d_∞ asymptotic value is defined as:

$$d_\infty = \lim_{n \to \infty} \frac{1}{n} \sum_{j=1}^{n} d_j. \tag{6}$$

Taking into consideration the quantitative characterizations of stretching properties by the λ, the evolution at the j^{th} iteration of the distance between the two trajectories is described in equation (7).

$$d_{j+1} = e^{\lambda} d_j = \Lambda d_j = e^{\lambda j} d_0. \tag{7}$$

After a sufficiently large number of iterations j, the folding process takes place and keeps the trajectories bound in the phase space. To take this phenomenon into account, we consider equation (8) as a first-order expansion of d_j and, in the hypothesis that $d_j < 1$ for any j, we include a second-order correction term (Γ) representing the folding action [13].

$$d_{j+1} = \Lambda d_j - \Gamma d_j^2 \tag{8}$$

The fixed points of equation (8) are

$$d_1 = 0 \tag{9}$$

and

$$d_2 = d_\infty = \frac{\Lambda - 1}{\Gamma}. \tag{10}$$

The characteristic values describing the evolution of nearby trajectories are therefore λ, Γ and d_∞, although only two of these are actually needed, because of the relationship in equation (10). It is important to notice that, while λ is sensitive only to the stretching mechanism, d_∞ is sensitive to both the stretching and the folding mechanisms; this is an important measure for the characterizations of chaos when the λ is not computed, or to distinguish between series which have the same λ.

3.2. **How to extract d_∞ from time series.** In the theoretical determination of λ and d_∞ as characterizing parameters for nonlinear systems, knowledge of the map $x_{j+1} = G(x_j)$ in the discrete domain as well as the differential equations in the continuous domain is fundamental.

When the laws of the systems under study are unknown and only experimental data are available, the need arises for a calculation of the d_j and of its asymptotic value d_∞ on generic time series.

On time series, trajectories starting from nearby points cannot be generated, but short sequences starting from nearby values at different times can be extracted. Given an original signal as a time series of L samples, all the sequences starting

from a point included in a d_0-radius boundary of a given $\bar{x}$ initial condition ($\bar{x} \pm d_0$) are extracted. They will represent for us the equivalent of the trajectories $x^{(i)}$.

The processing for calculating the d_j is performed using pairs ($x^{(i)}$, $x'^{(i)}$) among the selected sequences that meet certain constraints on parameters such as the initial slope and the minimum distance in time between them. The length in time of the sequences also needs to be fixed.

The initial slopes of a pair of sequences must agree in sign and must be close in value within a fixed tolerance expressed by the parameter p, therefore respecting the condition in equation (11).

$$|\dot{x}^{(i)}(0) - \dot{x}'^{(i)}(0)| = p * |\dot{x}^{(i)}(0)|. \tag{11}$$

The d_0 is chosen as small as possible according to the resolution of the acquisition system. The minimum distance in time between trajectories in pairs is fixed to avoid time correlation. The parameter p is chosen empirically, small enough that pairs of trajectories that are too different are discarded but not too strict so that a certain number of trajectories can be extracted in order to average sufficiently the d_j. The length of the time series is fixed in a way that, when the distance between them is calculated, both the stretching and the folding effects are taken into account, and the asymptotic behavior of the system can be studied. The d_∞, representing the asymptotic value of d_j, is then extracted and used as a parameter for characterizing the nonlinear dynamics of the system.

To characterize and to verify the reliability of the results from the newly developed algorithm, it was applied to a well-known numeric series. It was applied on the logistic map ($x_{n+1} = a * x_n * (1 - x_n)$), varying the control parameter a ($a = 3.5, 3.7, 3.8, 4$) in order to test different nonlinear dynamics.

The parameters of the algorithm were fixed as initial distance d_0=0.02, initial slope tolerance $p = 0.2$, length in time 1000 samples, and minimum distance in time between the trajectories 200 samples.

Figure 7 (a) shows, in semi-logarithmic scale, the d_j resulting from the application of the algorithm on the logistic series ($a = 3.7, 3.8, 4$) and presenting positive λ. The logarithm of d_j increases linearly with a rate proportional to the Lyapunov exponent, reaching asymptotically the d_∞ value. Figure 7 (b) shows d_j for the numeric series presenting a periodic behavior ($a = 3.5$). The d_j thus decreases to minus infinite (logarithm of zero) [14].

To study the effect of noise on the trend of the d_j and on the d_∞ value, the methodology presented here was applied to the logistic numeric series with $a = 4$, adding Gaussian Noise with variable variance (σ in the range between 0.01 and 0.50). As counterpart, the d_j curves were computed for a Gaussian distributed series with $\sigma = 1$ and for noise-free logistic numeric series. The d_j curves were compared as shown in Figure 7 (c). The d_j logarithmic curve relative to the Gaussian distributed series (black dashed line) rises very rapidly, going from -6 to -2 within one iteration and thus having a different trend from the one relative to the logistic series that rises from less than -7 to -1 within 5 iterations. The rising slope therefore can be considered as a parameter for the discrimination between the randomly distributed series and deterministic series. The curves d_j relative to the logistic map and adding noise at different rates represent intermediate conditions between the determinism of the logistic series (blue dashed line) and the random Gaussian distribution of the noise (black dashed line). The amplitude of the logistic series being equal to the unity, the variance value σ of the noise is a measure of

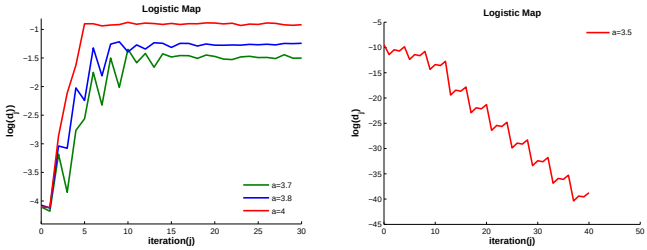

(a)

(b)

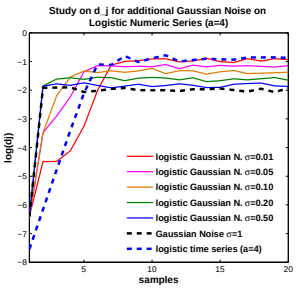

(c)

FIGURE 7. dj curves in logarithmic scale. (a) Logistic numeric series with chaotic behavior: green line for a=3.7, blue line for 3.8, red line for a=4. (b) Logistic numeric series with periodic behavior for a=3.5. (c) Logistic numeric series with a=4 with addition of Gaussian noise with variance σ vs. Gaussian noise numeric series with variance $\sigma = 1$.

the inverse of the signal to noise ratio. For low σ, and therefore for high signal-to-noise ratio, the d_j curves preserve the characteristic slopes, even though in the first iterations they have a dramatic increase. Conversely, considering high values for the variance ($\sigma = 0.20, 0.50$) with respect to the amplitude of the logistic map, the slope of the curves and their asymptotic value are close to the ones relative to the random series, therefore losing their characteristic initial dynamics. The curve trend and d_∞ value can be considered thus as fingerprints of deterministic behavior.

Furthermore, Figure 8 shows the consistency between the d_j resulting from the application of the developed algorithm on the logistic time series (red line) and the same curve computed using 30 pairs of trajectories obtained by the iterations of the known logistic map, starting from different initial conditions with an initial distance $d_0 = 0.02$ (blue line).

The consistency between the two curves shows the reliability of the developed algorithm for nonlinear iterative maps.

While taking into account the above-mentioned constraints, this method can be used for the characterization of time series coming from measurements performed

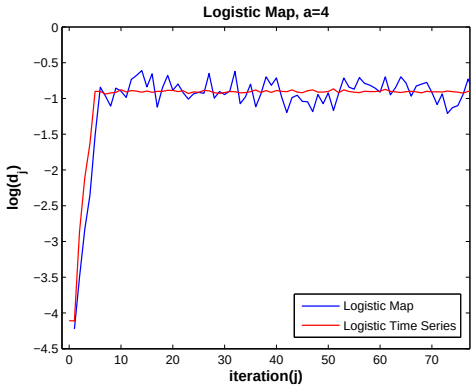

FIGURE 8. Comparison between the d_j calculated on the logistic through the logistic map and the logistic time series.

on real systems when the laws and structures are unknown and chaotic dynamics are suspected. Being computationally efficient, it is very applicable for large data sets.

4. **Spatio-temporal d_∞ maps on MEG data.** The implemented algorithm was applied to all 148 channels distributed on the scalp, as shown in Figure 1, for all the yogic breathing data sets. The MEG time series were normalized in the range between 0 and 1 in order to make the results independent from the signals amplitude. For each channel the entire period relative to each phase of the yogic protocol was considered. The implemented algorithm was applied on one-minute time windows, the d_j and the d_∞ calculated for each minute. The initial distance was fixed to d_0=0.006, the initial slope tolerance to $p = 0.2$, the length in time to 1000 samples and the minimum distance in time between the trajectories to 200 samples.

A first step verifying that the trend of the d_j and therefore the extracted d_∞ are a measure of determinism for MEG signals and do not come from random events was the performance of a surrogate test [20]. The surrogates data in this case were the random permutation of the original MEG time series. They maintain the same mean value and variance as the measured data.

One-minute periods were extracted for each phase (5^{th} minute for the rest phase I, 25^{th} minute for the exercise phase, 45^{th} minute for the rest phase II) and considerded two homologous channels of interest ($A116$ and $A127$ in Figure 1 (a)). The d_j computation was performed for both channels and for each phase, and the graphs are shown in Figure 9.

The curves relative to the surrogates, particularly three different permutations (colored solid lines), show a very sharp increasing trend while the curve relative to the data presents an initial dynamics leading to a smoother slope.

To verify that the d_j curves' trend and their initial slopes discriminate between data coming from random phenomena and the MEG data, a surrogate test was performed, and the distribution of the curves' slopes for N=20 surrogate data was compared to the one relative to the original data. The average slopes were computed between the point d_0 and the value d_j relative to the first occurrence of the value

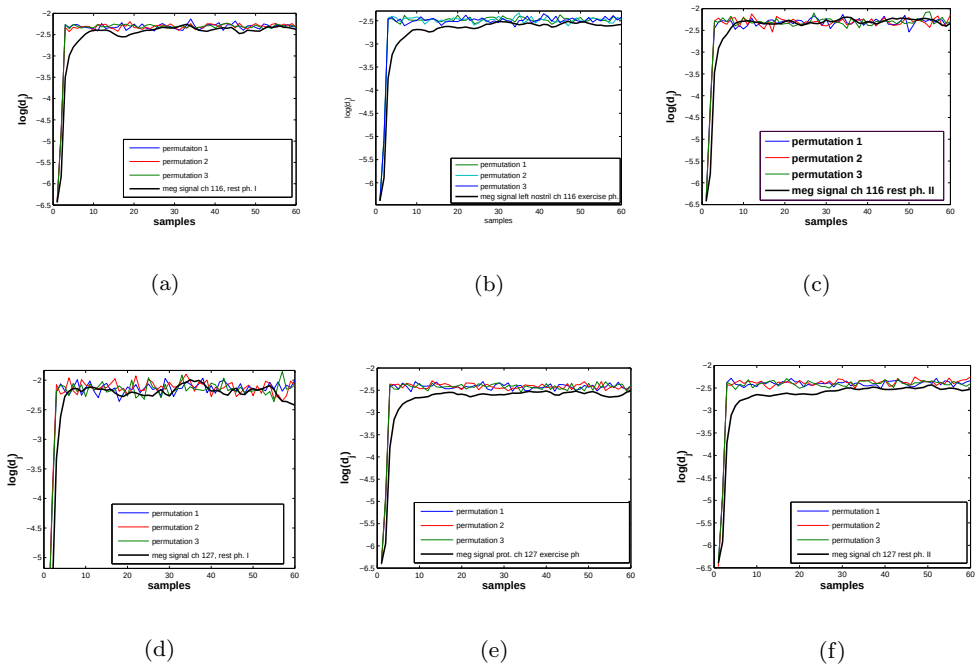

(a) (b) (c)

(d) (e) (f)

FIGURE 9. Comparison of the d_j for surrogate data and for original MEG data on one-minute period during the left nostril breathing protocol. Channel 116, (a) rest phase I, (b) exercise phase, (c) rest phase II. Channel 127, (d) rest phase I, (e) exercise phase, (f) rest phase II.

$d_{jMEAN} - 2 * d_{jSTD}$, where the d_{jMEAN} and the d_{jSTD} are respectively the mean and standard deviation of the d_j trajectory. This choice ensures that such slope is a measure of the transitory of the curve.

The results of the surrogate tests are shown in Figure 10 for channels A116 (a-c) and A127 (d-f)), and for the one-minute periods for each phase using the left nostril breathing protocol (data set 5). All the graphs show that the value relative to the slope of the d_j curve obtained from the original MEG data (red dashed line) is located out of the distribution of the slopes relative to the surrogate data. It can be concluded that the d_j curve trend and, in particular, its initial slope are discriminating between the original data and time series coming from random events. The asymptotic value of such curves can therefore be used as a measure of deterministic brain activity.

A second step following the significance test on the d_j curves' trend is the study of such curves relatively to the different phases of the yogic protocol in order to obtain a discriminating parameter.

Figure 11 (a), (b) shows respectively the logarithmic d_j curves for channels $A116$ and $A127$ of the left nostril breathing protocol. Figure 11 (c), (d) show the curves for the same channels for the right nostril protocol. The blue line refers to the rest phase I, the red line to the exercise phase and the green line to the rest phase II.

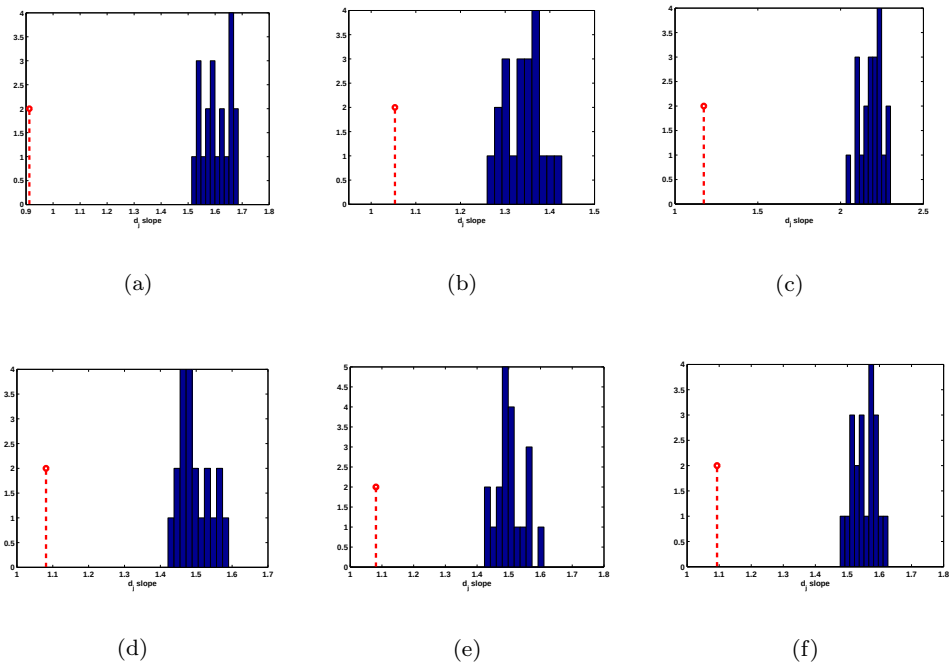

FIGURE 10. Surrogate test on MEG signal using permutated data. Distribution of the slopes of the d_j curves on one-minute time series: blue histogram for N=20 surrogate data; single value in red dashed line for the MEG original data. Channel 116, (a) rest phase I, (b) exercise phase, (c) rest phase II. Channel 127, (d) rest phase I, (e) exercise phase, (f) rest phase II.

The curves' rising trend is regular and reaches the asymptotic value after 10-20 samples; it is slower than the one occurring in the d_j coming from the Gaussian distributed noise. Furthermore, the curves do not tend to minus infinity, as occurs for periodic time series.

The two spatio-temporal maps are shown in Figure 12 for (a) the left and (b) the right nostril breathing protocols, for data sets 5 and 6. They give a representation of the whole-head MEG data d_∞ time evolution. The image's i^{th} column represents in a color code the time evolution by one-minute time-window steps of the logarithmic value of d_∞ for the i^{th} MEG channel. Some differences can be seen among the three different phases in the yogic protocol in different regions of the head and subtle variations can be observed between the left and right protocols.

It is also possible to notice the evolution in the dynamics characterized by the blue coded d_∞ in the rest phase II, which is visible in the cluster of channels from 120 to 148 for both the left and the right nostril protocols.This is an example of a gross variation of spatio-temporal patterns for a single channel or for channel clusters.

A further step in the visualization of the MEG signal dynamics is the spatial representation of the average logarithmic value of the d_∞ through the three phases. The d_∞ head maps were obtained averaging the spatio-temporal maps over the

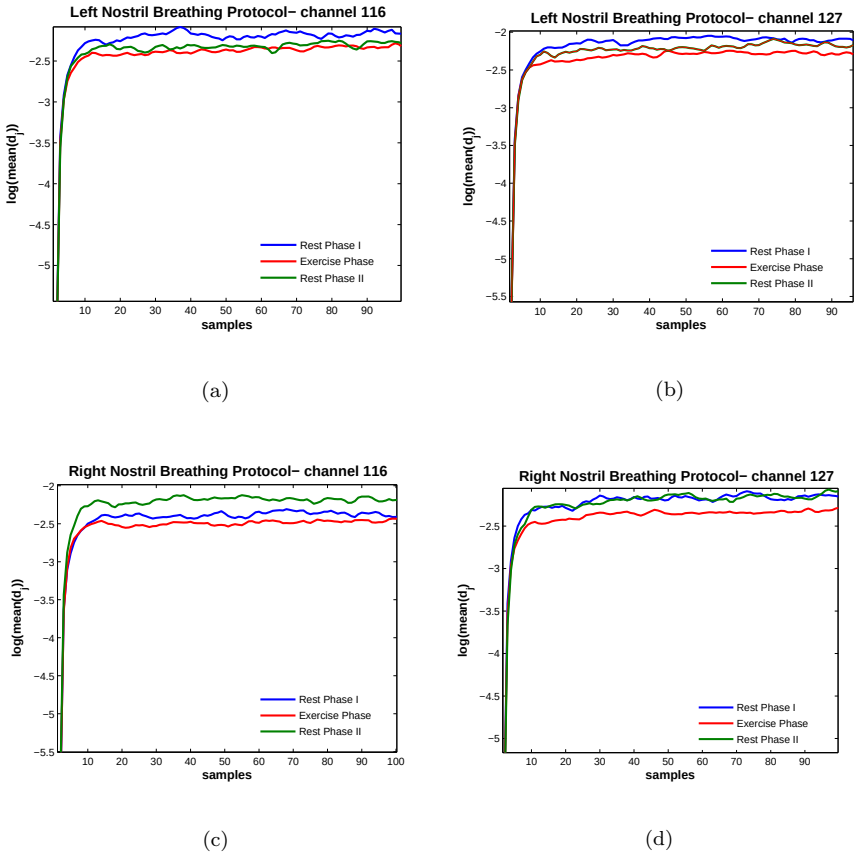

FIGURE 11. d_j in two homologue channels of interest 116 and 127. (a,b) Left nostril breathing protocol.(c,d) Right nostril breathing protocol

three phases as it is described in Section 2.2. Figure 13 shows the head maps for each phase of the data sets 5 and 6.

Figure 13 (a)-(c) represents the d_∞ patterns respectively of the rest phase I, exercise phase, and rest phase II relative to the left nostril breathing protocol (data set 5), whereas Figure 13 (d)-(f) is relative to the same phases in the right nostril breathing protocol (data set 6). A comparative study of the d_∞ in the three phases was performed in order to investigate the effect that both the left nostril and right nostril breathing exercises have on the brain. It is worth noting how the average d_∞ head patterns change through the three phases. In rest phase I the patterns represent an activity characterized by a high d_∞ value spread in the temporal and parietal lobes and low d_∞ values in the peripheral parietal lobes. In the exercise phase the pattern is characterized by a very concentrated area with high d_∞ in the central part of the scalp with two narrow branches going to the parietal lobes and resembling the sensory-motor cortex. This might be considered

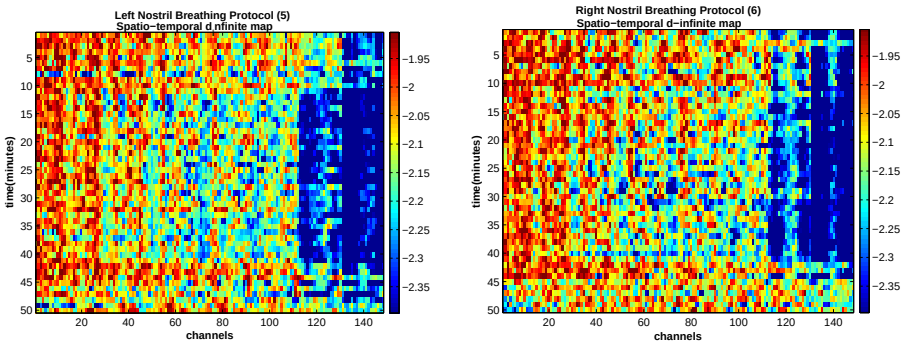

(a) (b)

FIGURE 12. Spatio-temporal d_∞ maps. (a) Left nostril breathing protocol (5). (b) Right nostril breathing protocol (6).

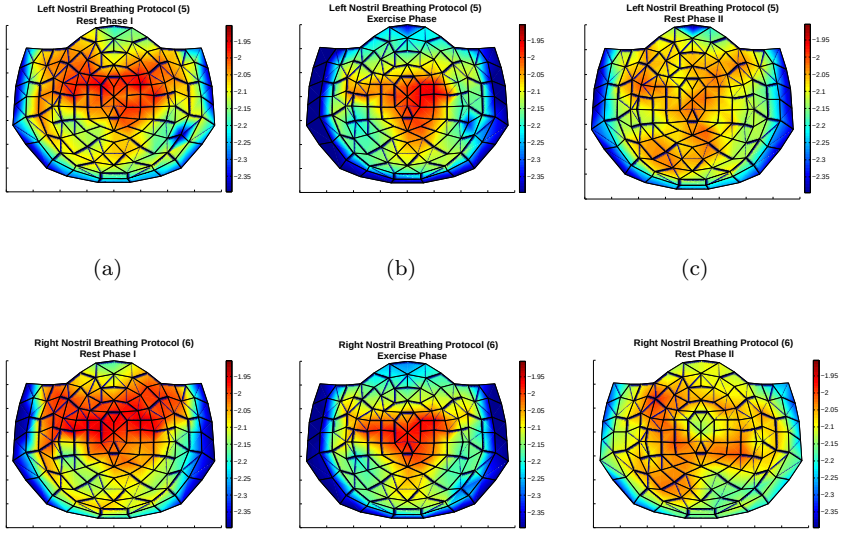

(a) (b) (c)

(d) (e) (f)

FIGURE 13. Average d_∞ head maps. Left nostril breathing protocol (5). (a) Rest phase I. (b) Exercise phase. (c) Rest phase II. Right nostril breathing protocol (6). (d) Rest phase I. (e) Exercise phase. (f) Rest phase II.

an effect produced by the breathing exercise when the subject's concentration is focused on the breathing movement and sensory feedback.

A low d_∞ area is distributed in the narrow peripheral area of the whole scalp. This might be considered reasonable since low d_∞ values characterize periodic time series and the peripheral areas are the most affected by the heart beat. In rest phase II the pattern is more diffused over the whole scalp without the same concentration of high or low peaks of d_∞.

However, there appears to be higher d_∞ in the left half of the brain in the right nostril protocol, and the opposite in the left nostril protocol. The two rest phase II patterns appear to have the greater asymmetry, respectively to rest I and the exercise phases here.

At first sight, the spatial patterns shown in Figure 13 do not show striking differences between the left and the right nostril breathing protocols. The difference between each phase of the two protocols is therefore performed in order to investigate a potential difference.

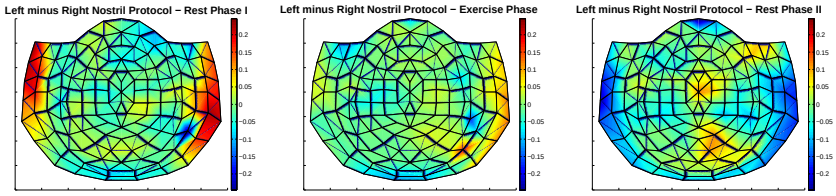

(a) (b) (c)

FIGURE 14. Difference between the average d_∞ value of the two different breathing protocols. (a) Rest phase I. (b) Exercise phase. (c) Rest phase II .

Figure 14 (a)-(c) shows the difference between the average d_∞ map for the rest phase I, exercise phase, rest phase II, respectively, in the left and the right nostril breathing protocols. Figure 14 (b, c) respectively show the corresponding differences between the average d_∞ map relative to the exercise phase and the rest phase II. Asymmetry can be seen during the exercise phase in the right parietal lobe, where the d_∞ is higher during left nostril breathing than during right nostril breathing.

To verify the consistency of the spatio-temporal patterns observed in data sets 5 and 6 in Figure 13, the data sets from the successive experiments for data set 7-10 (Table 1) are shown in Figures 15 and 16.

Through all the experiments during the exercise phase, it was found that the highest values of d_∞ are distributed in the center of the scalp, with two branches towards the parietal lobes. Also the more evenly distribution of d_∞ values in the rest phase II results are consistent through all the experiments in the three-month period. However, again a greater left hemispheric value is apparent for d8 in the right nostril protocol, with the reverse in the left nostril protocol.

It is worth noting how the values of the spatial distribution become more uniform in the data sets 7 and 8 (Figure 15) and 9 and 10 (Figure 16) compared to the ones relative to the data sets 5 and 6 (Figure 13) in all the three phases, especially in

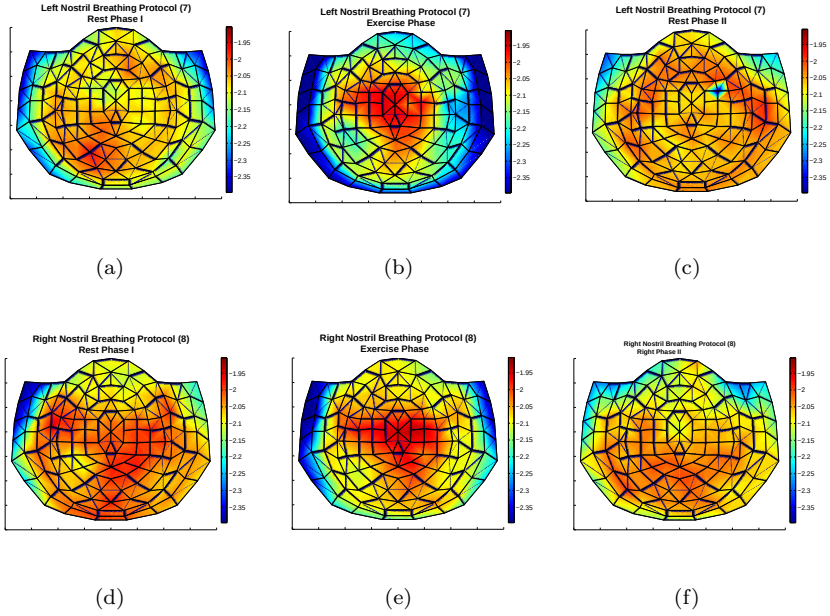

FIGURE 15. Average d_∞ head maps. Left nostril breathing protocol (7). (a) Rest phase I. (b) Exercise phase. (c) Rest phase II. Right nostril breathing protocol (8). (d) Rest phase I. (e) Exercise phase. (f) Rest phase II.

rest phase I and in rest phase II. This implies that the practice of the yogic protocol may have effects over the long run.

In comparing the d_∞ spatio-temporal patterns with the power distribution patterns, it is apparent that they can be used to represent different information. The functional and anatomical correspondence of the spatial patterns observed with the d_∞ maps does not occur with the power distribution maps. In the d_∞ maps the residual effect of the exercise phase on the rest phase II are more clearly visible by the smoothing of the d_∞ distribution. In contrast, the difference between the left and the right breathing protocol is more evident in the power distribution. Therefore, it appears that the information from both approaches can complement each other.

5. **Conclusions.** A method to extract the d_∞ directly from time series has been developed. It can be used as a method for the characterization of nonlinear systems and in particular of spatio-temporal nonlinear dynamics in MEG signals. This approach can be used for the characterization of time series coming from measurements performed on real systems when the laws and structures are unknown and chaotic dynamics are suspected.

The algorithm was applied to whole-head 148-channel MEG data during a structured yogic breathing meditation technique. This procedure was performed in an effort to capture the residual brain effects that supposedly differ from left or right nostril breathing [19].

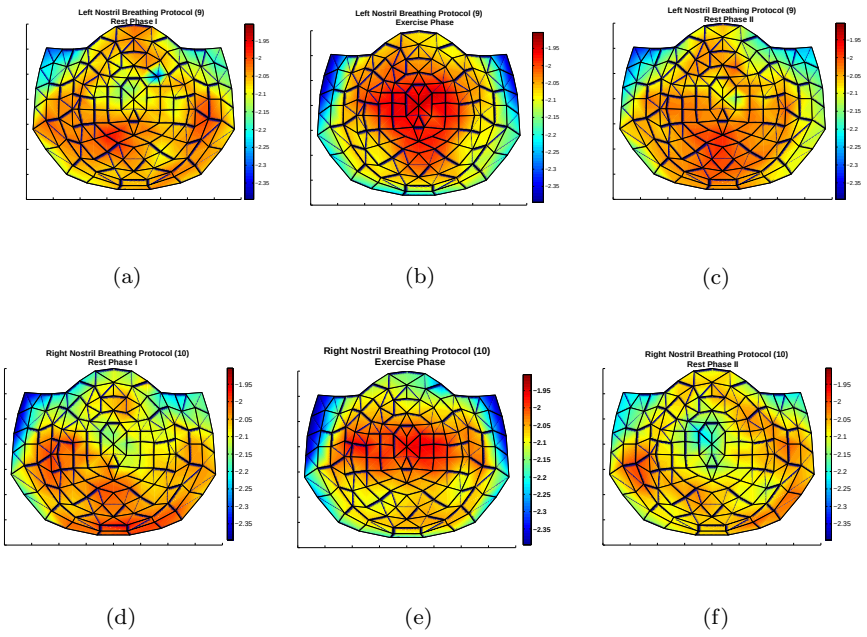

FIGURE 16. Average d_∞ head maps. Left nostril breathing protocol (9). (a) Rest phase I. (b) Exercise phase. (c) Rest phase II. Right nostril breathing protocol (10). (d) Rest phase I. (e) Exercise phase. (f) Rest phase II.

Spatio-temporal distributions of the d_∞ are calculated on the normalized MEG signals and they are presented on head maps. Dramatic differences between the d_∞ distributions on the head map during the three different phases arise that were not clearly featured in the power spatio-temporal plots. Since an enormous amount of data results from 148 channels over such long recording periods, it is very important to have a computationally efficient approach for signal processing. We propose the d_∞ characterization as a promising, convenient, and complementary method to that of MEG power alone. We believe this will help lead to a better understanding of temporal and spatial patterns that are not only related to higher power activity but also to those of lower power that are also essential for the decoding of the brain's complexity. A global spatial and time representation of brain activity with this approach may be helpful for diagnostics, analysis of sensory evoked activities, and for other purposes.

REFERENCES

[1] W. J. Freeman, TUTORIAL ON NEUROBIOLOGY: FROM SINGLE NEURONS TO BRAIN CHAOS. The International Journal of Bifurcation and Chaos 2(3) (1992) 451-482.
[2] E. M. Izhikevich, DYNAMICAL SYSTEMS IN NEUROSCIENCE: THE GEOMETRY OF EXCITABILITY AND BURSTING.The MIT Press, Cambridge, 2006.
[3] C. Uhl, ANALYSIS OF NEUROPHYSIOLOGICAL BRAIN FUNCTIONING. Springer, Berlin, 1998.
[4] H. Haken, NONLINEARITIES IN BIOLOGY: THE BRAIN AS AN EXAMPLE. Lecture Notes in Physics 542 (2000) 427-445. Springer Berlin/Heidelberg GmbH, 2000.

[5] S.Makeig, A.J.Bell, T.P. Jung, T.J.Sejnowski, Independent component analysis of electroencephalic data. in Advances in neural information processing systems 8 (1996) 145-151. MIT Press, Cambridge, 1996.

[6] A. Fuchs, V. K. Jirsa, and J. A. S. Kelso, Theory of the Relation between Human Brain Activity (MEG) and Hand Movements. NeuroImage 11 (2000) 359-369.

[7] A. Fuchs, V. K. Jirsa, and J. A. S. Kelso, Spatiotemporal forward solution of the EEG and MEG using network modelling. IEEE Transaction on Medical Imaging, 21(5) (2002).

[8] E. Pereda, R. Q. Quiroga , J. Bhattacharya, Nonlinear multivariate analysis of neurophysiological signals. Progress in Neurobiology 77 (2005) 137.

[9] Z. J. Kowalik, A. Schnitzler, H. J. Freund, O. W. Witte, Local Lyapunov exponents detect epileptic zones in spike-less interictal MEG recordings. Clinical Neurophysiology, 112 (2001) 60-67.

[10] G. Nolte, T. Sander, A. Lueschow, B. A. Pearlmutter, Nonlinear time series analysis of human alpha rhythm (2002). [Accessed August 2006] Available from: http://www-bcl.cs.may.ie/ bap/papers/biomag-2002-nonlinear.pdf.

[11] U. Parlitz, Nonlinear Time-Series Analysis in Nonlinear Modeling Advanced Black-Box Techniques Eds. J.A.K. Suykens and J. Vandewalle Kluwer Academic Publishers, 1998.

[12] A. Bonasera, M. Bucolo, L. Fortuna, A. Rizzo, The d_∞ parameter to characterise chaotic dynamics . Neural Networks, 2000. IJCNN 2000, Proceedings of the IEEE-INNS-ENNS International Joint Conference on, 5 (2000) 24-27 .

[13] A. Bonasera, M. Bucolo, L. Fortuna, M. Frasca, A. Rizzo, A New Characterization of Chaotic Dynamics: The d_∞ Parameter, Nonlinear Phenomena in Complex Systems, 6(3) (2003) 779-786.

[14] S. H. Strogatz, Nonlinear Dynamics and Chaos. Perseus Book, Cambridge, Massachusetts. Webster J.G.. Medical Instrumentation, Wiley, 1998.

[15] M. Bucolo, M. La Rosa, M. Frasca, L. Fortuna, D. Shannahoff-Khalsa, R. L. Schulz, J. A. Wright, Independent Component Analysis of Magnetoencephalography Data. Conference of IEEE Engineering Medicine and Biology Society (EMBC 01), Istanbul, 2001.

[16] D. Shannahoff-Khalsa, L. E. Ray, S. Levine, C .C. Gallen, B. J. Schwartz, J. J. Sidorowich, Randomized Controlled Trial of Yogic Meditation Techniques for patients with Obsessive Compulsive Disorders. CNS Spectrums: The International Journal of Neuropsychiatric Medicine, 4(12) (1999) 34-47.

[17] S. Baglio, M. Bucolo, L. Fortuna, M. Frasca, M. La Rosa, D. Shannahoff-Khalsa, MEG Signals Spatial Power Distribution and Gamma Banda Activity in Yoga Breathing Exercises. Proceeding of the Secocond Joint EMBS/BMES Conference, Houston, TX, USA, 2002.

[18] G. Bucolo, M. Bucolo, M. Frasca, M. La Rosa, D. Shannahoff-Khalsa, M. Sorbello, Spatial Modes in Magnetoencephalography Spatio-Temporal Patterns. Proceedings of the 25^{th} Annual International Conference of the IEEE EMBS, Cancun, Mexico, 2003.

[19] D.S. Shannahoff-Khalsa, Unilateral forced nostril breathing: Basic science, clinical trials, and selected advanced techniques. Subtle Energies and Energy Medicine Journal 12(2) (2001) 79-106.

[20] Thomas Schreiber, Andreas Schmitz Surrogate time series. Physica D 142 (2000) 346382.

Received on February 27, 2006. Accepted on June 28, 2006.

E-mail address: fsapuppo@diees.unict.it
E-mail address: elenaumana@tiscali.it
E-mail address: mfrasca@diees.unict.it
E-mail address: manuela.la-rosa@st.com
E-mail address: dsk@ucsd.edu
E-mail address: lfortuna@diees.unict.it
E-mail address: mbucolo@diees.unict.it